

CORROSION PERFORMANCE OF STAINLESS STEEL CLAD REBAR IN SIMULATED PORE WATER AND CONCRETE

Fushuang Cui, Alberto Sagüés
Department of Civil and Environmental Engineering
University of South Florida
4202 East Fowler Ave ENB118.
Tampa, FL 33620

ABSTRACT

The corrosion performance of stainless steel clad reinforcing bar (SCR) was investigated. Corrosion potential of SCR in various alkaline media as a function of time was measured periodically and corrosion rates were estimated using Electrochemical Impedance Spectroscopy (EIS). At room temperature, SCR without cladding breaks was free of corrosion for up to one year in all the testing conditions: saturated $\text{Ca}(\text{OH})_2$ solutions (SCS, pH ~12.6), simulated pore solution (SPS, pH ~13.6), simulated carbonated concrete pore solution (CPS, pH <10) (each with 15 wt% chloride by the end of test), and concrete with chloride up to 8% chloride by weight of cement. SCR without cladding breaks also remained passive at 40 °C in SCS with 15% chloride and in concrete with 8% chloride. SCR with a 1 mm hole corroded actively in SCS with 15% chloride. The results suggest that carbon steel exposed by the small hole was corroding actively at a high local rate. A model for SCR with a single cladding break at one cut-end in concrete was modeled using a finite differences approach. Calculations indicated that the resistivity of concrete and size of cladding breaks were critical parameters in establishing the rate of corrosion, and that corrosion of SCR with sub-millimeter breaks in high quality concrete would cause concrete cracking only after long service times.

Keywords: stainless steel, cladding, EIS, chloride threshold, corrosion, concrete, rebar

INTRODUCTION

Austenitic stainless steel (SS) rebars have shown very promising corrosion performance in chloride-contaminated concrete⁽¹⁻⁶⁾ but at a higher cost than conventional plain carbon steel (CS) rebar. Stainless steel clad rebar (SCR)⁽⁷⁾ with a carbon steel core offers the potential for performance comparable to that of solid SS rebar but at a much lower cost. However, SCR is vulnerable to corrosion at cladding breaks that may result from local mechanical damage or unprotected cut ends. Upon chloride contamination of the surrounding concrete, an intense galvanic couple may develop between the exposed carbon steel and the surrounding, still passive, stainless steel. These conditions can be especially promoted in marine service^(8,9). The resulting extent of corrosion is a function of the amount of the base steel exposed and the surrounding stainless steel, the polarization characteristics of both, and the properties of the surrounding concrete.

This work examined these issues by characterizing the corrosion behavior of SCR in the sound condition (no cladding breaks), and with intentionally introduced breaks, in various simulated concrete pore solutions and concrete to which controlled amounts of chloride ions were introduced. The results were input to a simplified model to estimate the extent of corrosion that may result from the corrosion macrocell between a small spot of carbon steel exposed at a cladding break and the rest of a reinforced concrete cylinder.

EXPERIMENTAL

Materials and Preparation

The Stainless Steel Clad Rebar (SCR) stock investigated was No.5 (16 mm diameter), corrugated, with a typical 0.8 mm thick cladding of Type 316L SS, and manufactured using the Nuovinox Process⁽⁷⁾. Specimens, 5 or 10 cm long, were cut out for evaluation. Electric contact was made through copper wires placed at one end which then was covered by specially designed mortar caps to prevent crevice corrosion, which is otherwise frequently observed at the junction with an epoxy cap. The other end was terminated by one of the following methods: A, a proprietary stainless steel cap; B, a welding overlay; C, another mortar cap.

Methods A and B were to evaluate two proposed capping methods for SCR cut-ends in field construction. Method C was used to evaluate the behavior of the side surfaces without observing a crevice-corrosion effect. Figure 1 shows the configuration of specimens. The mortar caps were prepared using the following procedures:

1. cover the exposed CS with a thin layer of two-component epoxy;
2. then cast the cut-end in ordinary Portland cement mortar (w/c/sand: 0.5/1/2) forming a cap with a cover thickness of ~8 mm;
3. after 1 day curing, demold the cap, and apply two layers of Pilgrim Plastic two-component epoxy coating to all the surfaces of the cap to minimize chloride penetration.

Test Conditions

1. SCR without cladding breaks

1.1. Test conditions in model solutions

SCR specimens were tested in saturated $\text{Ca}(\text{OH})_2$ solution (SCS, pH~12.6), simulated carbonated concrete pore solution (CPS, pH~9.7), and simulated concrete pore solution (SPS, pH~13.6). The composition of CPS was based on water chemistry calculation by considering an open aqueous carbonated system⁽¹⁰⁾. Table 1 summarizes the composition and pH values of all the test solutions.

With duplicate SCR specimens immersed in the testing solutions, chloride ions were added stepwise in the form of reagent grade NaCl. After each addition step the electrochemical condition of the steel was assessed as indicated below. If the steel was found to be passive, more chloride ions would be introduced to the solution. Additions continued until active behavior developed, or until the NaCl concentration reached 15 wt% (~5M) which is close to the solubility limit of NaCl. The open circuit potentials (OCP) of rebar samples were measured periodically using a Saturated Calomel Electrode (SCE) as reference electrode. To estimate corrosion rate, Electrochemical Impedance Spectroscopy (EIS) was performed after the E_{oc} had stabilized (at least 7 days), using an Activated Ti Rod (ATR)⁽¹¹⁾ as a temporary reference electrode and a high-density graphite rod as the counter electrode. The test frequency range was from 300 kHz to as low as 0.3 mHz. The equivalent circuit shown in Figure 2.a was used to fit the EIS spectra and obtain R_p , R_s , Y_0 and n . The values of R_p were used to calculate a nominal corrosion current density $i_{nom} = B/R_p$ ⁽¹²⁾ ($B=52$ mV for passive specimens and 26 mV for active specimens). Test temperature was normally 22 ± 2 °C. Additional experiments were conducted as well in SCS at 40 ± 2 °C: To minimize temperature effect on the potential of SCE, a salt bridge was used between the SCE and the high temperature SCS.

1.2 Test conditions in concrete with chlorides

7.5 x 12.5 x 12.5 cm concrete prisms with 5 or 8% chloride by weight of cement were cast in duplicate. The concrete mix design is a modification of Florida DOT Class IV concrete^(13,14): cement (type I) 390 kg/m^3 , water 175.5 kg/m^3 ($w/c=0.45$), Fine Aggregate 706.5 kg/m^3 , Coarse Aggregate 986.4 kg/m^3 . Each concrete prism had two SCR bars: one Type B and one Type C, while an ATR electrode was placed in the middle as reference electrode and an activated Ti mesh was laid at the bottom as counter electrode. Figure 3.a shows the layout of a concrete specimen before casting. Normal test temperature was 22 ± 2 °C. At this temperature and for the type of concrete used, the 8% composition corresponds to pore water nearly saturated with chloride ions.

Similar to the model solution tests, OCP and EIS techniques were employed to examine corrosion behavior of SCR in concrete. To evaluate the effect of temperature on SCR corrosion behavior in concrete, the concrete specimens with 8% chloride were moved into a 40 ± 1 °C 100% relative humidity chamber after 8 months' exposure in normal laboratory conditions.

2. SCR with cladding breaks

2.1 Test conditions in model solutions

To study corrosion behavior of SCR with cladding breaks, a 1mm ϕ hole near the middle of the exposed side surface of the 5 cm long type C SCR specimen was made. The hole was drilled so that the full diameter of the bit just penetrated the entire cladding thickness, exposing a shallow conical CS surface at the exposed side surface. This rebar specimen was then immersed in SCS. After 7 days pre-passivation, chloride was introduced in one step to reach a concentration of 15 wt%. OCP and EIS measurements were performed periodically. EIS spectra were interpreted using the circuit shown in Figure 2.b. Estimated R_p values were then used to calculate corrosion rates as described above.

Triplicate specimens were used. Additional tests with model solutions are in progress and will be reported later.

2.2 Test conditions in concrete with chlorides

Two 7.5 x 7.5 x 12.5 cm concrete prisms with 8% chloride by weight of cement were cast using the same concrete proportions indicated earlier. Each concrete prism had one 10 cm long type C specimen with a 1mm ϕ hole near the middle. The preparation of the holes was the same as that described in Sec. 2.1. As shown in Figure 3.b, one ATR electrode was placed next to the rebar to serve as reference electrode and an activated Ti mesh was placed at the bottom of concrete mold as counter electrode. Similar testing plan to that of Sec. 2.1 was employed to characterize these SCR specimens and the electric circuit shown in Figure 2.b was used to interpret EIS data.

RESULTS AND DISCUSSION

1. SCR without cladding breaks

1.1 Solution test in model solutions

Experiments were performed on duplicate specimens and showed similar behavior. Figure 4.a shows that the potentials (E_{oc}) of SCR with isolated ends increased with time in saturated $\text{Ca}(\text{OH})_2$ solution (SCS) despite the addition of chloride ions nearly up to the solubility limit. By the end of the test the average E_{oc} was still about -80 mV. EIS results and the noble values of E_{oc} both suggested that the SCR specimen surfaces were passive throughout the testing period. Similar behavior was observed in simulated carbonated concrete pore solution (CPS) and simulated concrete pore solution (SPS) (shown in Figure 4.b). As observed in Figure 4, the E_{oc} values of SCR were higher when the pH of the testing solution was lower. For example, at day 260, the E_{oc} of SCR in CPS, SCS and SPS are 30, -90, -124 mV respectively. This observation may be attributed (at least in part) to the dependence of the redox $\text{O}_2/\text{H}_2\text{O}$ system on pH. The pH values of the solutions noticeably decreased with the addition of chloride. For example, when chloride concentration reached 15 wt%, the pH of CPS, SCS and SPS were 8.6, 12.1, 13.1 respectively while the initial values were 9.7, 12.5 and 13.6. This behavior is likely at least in part the result of increased ion strength and consequently decrease in OH^- activity⁽¹⁵⁾. The pH range in these tests was nevertheless representative of typical pH values encountered in field concrete applications^(16,17) suggesting that SCR in concrete also has very high corrosion resistance to chloride contamination and in agreement with the findings from the tests in concrete shown below.

Figure 4 also shows that E_{oc} of SCR increased with time over a relatively long time period (~1 year). Because of the time scale (Figure 5) the potential increase is not likely related to the addition of Cl^- , but rather reflects increasingly mature passivity of the specimen surface.

Figure 6 summarizes the E_{oc} of SCR with different termination methods as a function of time in SCS while chloride level was increased stepwise up to 15 wt%. Although initial E_{oc} values varied, they eventually reached similar values (~-80 mV) after the SCR specimens have been in SCS with 15 wt% chloride for more than 6 months. EIS results and the noble potential values both indicated that all the specimen surfaces were passive throughout the testing period.

When the temperature of the testing solution was raised from room temperature (22 ± 2 °C) to 40 ± 2 °C, as shown in Figure 7, the potentials of SCR in SCS were frequently higher than those at room

temperature. Nonetheless, as in the room temperature tests, SCR remained passive even when Cl^- level reached 15 wt%.

1.2 Concrete tests

Figure 8 shows the E_{oc} of SCR with isolated ends or terminated with an SS cap in concrete with 5 wt% ($\sim 19.5 \text{ kg/m}^3$) chloride by weight of cement. Starting from relatively low potentials ($< -200 \text{ mV}$), the potentials increased with time and gradually stabilized at values between -120 and -140 mV . The increase of E_{oc} and EIS results both indicated passivity throughout the testing period.

Figure 9 shows that SCR specimens remained passive as well in concrete with 8 wt% Cl^- ($\sim 31.2 \text{ kg/m}^3$) at room temperature. After ~ 280 days' exposure, the specimens were moved into a 100% relative humidity chamber kept at 40°C . After that transition all potentials dropped significantly and showed more scatter. However, EIS test results indicated passive behavior up to the last available data sampling. Testing continues.

Figure 10 shows typical EIS diagrams of passive SCR in high chloride contents. For these conditions, a 0.3 mHz lowest test frequency was chosen to limit EIS test duration and retain sufficient system stability during the test. However, this frequency limit was often not low enough for spectral components with long characteristic times. The resulting high R_p estimate thus only served as a qualitative indicator of high passivity.

The chloride levels used both in solutions and concrete corresponded to nearly chloride-saturated pore water, at the limit of the chloride bearing capacity of concrete. The specimens remained passive in these extremely corrosive environments for up to one year, which is a promising indication of performance for SS316L SCR without cladding breaks and with either welded or capped end terminations. However, continuation testing and analysis is important to ascertain whether this performance will be sustained over the much longer time frame of service in an actual structure.

From a testing technique standpoint, the results also showed that the mortar cap termination method used here successfully prevented crevice corrosion over a rather long period (>1 year), a significant improvement over previous experiments using cast epoxy ends⁽¹⁸⁾.

2. SCR with cladding breaks

2.1 Solution tests

As shown in Figure 11, the E_{oc} values of SCR with a $1 \text{ mm } \phi$ hole were between -200 and -100 mV in chloride-free SCS, and dropped quickly to values lower than -500 mV upon the addition of 15 wt% chloride. One of the three specimens showed some recovery after ~ 160 days. Nominal local corrosion rates (Figure 12) were calculated using values of R_p estimated from EIS data (exemplified later in Figure 17) per the equivalent circuit in Figure 2.b and the surface area of the drilled hole. By the end of the test values were $\sim 10 \mu\text{A/cm}^2$ for the specimen that showed some recovery and between 100 and $1000 \mu\text{A/cm}^2$ for the other two. The results suggest that some favorable plugging effect by corrosion product accumulation at the opening may be taking place.

Preliminary evaluation of corrosion morphology is in progress. After ~ 280 days immersion, two of the three specimens were taken out and metallographically sectioned using a precision saw⁽⁹⁾. As shown in Figure 13.a, before sectioning the corrosion products filled the drilled hole and stuck out

normal to the surface of the specimen even though it was placed vertically. Figure 13.b shows that in these specimens the corrosion of exposed CS propagated in a roughly hemispherical shape with some preferential corrosion at the CS/SS interface. Corrosion in the hemispherical region had penetrated ~1mm in average, and the estimated volume loss of CS was 0.0021 cm^3 (or a mass of ~0.016 g), which corresponds to an average corrosion rate of ~240 $\mu\text{A}/\text{cm}^2$ in reasonable agreement with the EIS estimates. Metallographic examination of additional specimens exposed to model solutions was initiated. Indications of further damage progression at the CS/SS interface of some of the specimens are being currently assessed.

2.2 Concrete tests

As shown in Figure 14 and 15, only one of the two specimens showed clear signs of active corrosion development during the test period (and even then with some indications of later recovery), despite the very high chloride content of the concrete. As shown in Figure 16, the value of the concrete resistance for the anode, R_h , decreased during the most active period, as expected from the corresponding localization of current. The recovery after activation might be attributed to plugging by corrosion products. Testing continues to assess behavior over a longer time frame.

Figure 17 shows typical EIS spectra of SCR in concrete (interpreted using the equivalent circuit in Figure 2b). An example of EIS results in SCS is shown for comparison.

MODELING

The SCR lateral surface, or SCR terminated by a SS cap or a welding overlay showed high corrosion resistance in the tests to date. However, as expected, CS exposed at cladding breaks corroded actively in chloride-contaminated media. This corrosion problem could be even more serious in field applications because of the formation of a galvanic cell with a large cathode/anode ratio. To investigate the possible extent of corrosion, a numerical model was developed to calculate the current distribution between a small anodic spot and the large surrounding cathodic area. This break could represent, for example, a small residual flaw where a weld overlay failed to completely cover a rebar cut end.

The system studied was a reinforced concrete cylinder with an SCR element embedded axially (Figure 18). The concrete cover was 7.5 cm everywhere. It was assumed that there was a circular cladding break at the center of the cut-end termination, as it may take place due to a small closure weld imperfection. The exposed CS was assumed to be already undercut by some corrosion so that a CS area 4 times that of the break was exposed to the internal electrolyte, as in Figure 13 b. The rest of the SS rebar surface was considered to be passive. The concrete was treated as homogeneous with uniform effective oxygen diffusion coefficient D_{O_2} and electrical conductivity σ_c ⁽¹⁹⁾. The effective oxygen concentration was considered to be constant on all the external surface of concrete cylinder. The concrete cylinder was truncated at 1m away from the end of cylinder, at which distance the results showed that macrocell coupling effect became much smaller.

The CS exposed by the clad break was assumed to be in the active condition, due to chloride contamination of the adjacent concrete and chloride accumulation inside the undercut. The net current density i_a of the CS inside the undercut and the net cathodic current density i_c on the SS surface were assumed to be given respectively by:

$$i_a = i_{oa} 10^{\frac{E_{oa} - E}{b_a}} - i_{oc} \frac{C_s}{C_o} 10^{\frac{E - E_{oc}}{b_c}} \quad (1)$$

$$i_c = i_{oc} \frac{C_s}{C_o} 10^{\frac{E-E_{oc}}{b_c}} - i_p \quad (2)$$

so that both the CS anodic and the SS cathodic processes were considered to be determined by Butler-Volmer kinetics, with Tafel slopes b_a and b_c , exchange current densities i_{oa} and i_{oc} , equilibrium potentials E_{oa} and E_{oc} and local electrode potentials E . The cathodic reaction rate included oxygen concentration dependence with C_s as the concentration at the SS surface and C_o the concentration at the external concrete surface (oxygen concentration is expressed in terms of mole per cubic meter of pore water, as in Ref. 19). A passive anodic dissolution current density i_p was assumed to be present at the SS surface. Results from the electrochemical measurements were used to abstract input values (shown in Table 2) of the electrochemical parameters except for the anodic reaction for which a nominal Tafel slope of 0.06 V/dec was assumed. The i_{oa} value was then adjusted to obtain a corrosion current matching that estimated from the EIS tests (at the appropriate potential). All magnitudes were assigned the appropriate sign as needed.

It was assumed that both the oxygen concentration and electrical potential distributions had reached a steady state. Given that electrical conductivity and oxygen diffusion coefficient were assumed to be constants, the Laplace equation applied to both variables:

$$\nabla^2 E = 0 \quad (3)$$

$$\nabla^2 C = 0 \quad (4)$$

Boundary conditions were applied linking diffusional oxygen flux at the metal surface with the concentration and potential dependant rate in Eq. (2), as well as applying ohm's law at each point of the surface to match the difference in net current densities given by Eqs. (1) and (2) as described in earlier publications⁽¹⁹⁾. Conditions at the break were implemented by treating the exposed CS as being flush with the rest of the surface, but assigning to that region an exchange current density i'_{oa} four times greater than i_{oa} to reflect the greater area of the undercut. This approximation reflects the assumption that inside the undercut electrolytic conductivity is expected to be high and more or less equipotential conditions apply. The model calculations were implemented using a finite difference method formulated for cylindrical coordinates as described elsewhere^(19, 20).

The base case was chosen to represent a system with large cathode/anode ratio and high quality concrete: $\rho = 30 \text{ k}\Omega\cdot\text{cm}$, $D_{O_2} = 10^{-4} \text{ cm}^2/\text{s}$, $C_o = 3 \cdot 10^{-7} \text{ mol}/\text{cm}^3$, and $r_o = 0.05 \text{ cm}$. The assumed nominal anodic passive current density at the SS surface was $i_p = 4 \cdot 10^{-9} \text{ }\mu\text{A}/\text{cm}^2$. This value, combined with the choice of cathodic polarization parameters, would yield an $E_{oc} = -0.16 \text{ V}$ for the SS surface if it were subject only to local cell action (roughly approximating the experimental values for sound surface specimens). The variables σ_c , r_o , i_{oa} and i_{oc} were parameterized to examine the sensitivity of corrosion rate to these factors.

Calculation Results and Discussion

Figure 19 shows the calculated potential distribution and the corresponding current densities along the SCR surface. As shown in Figure 19.a, the potential increases rapidly from $\sim -0.5 \text{ V}$ at the anodic break region to -0.2 V at the perimeter of the rebar termination. Consequently, as shown in Figure 19.b, the cathodic current density decreases dramatically with distance to the anode. The anodic current density at the break is in the order of $100 \text{ }\mu\text{A}/\text{cm}^2$, in agreement with EIS results and mass loss

estimation. When the distance to the anode increases further along the bar in longitudinal direction, (Figure 19.c and d), the potential changes slowly and the cathodic current density gradually decreases to approach the value of i_p .

The corrosion at the break is expected to result in accumulation of expansive corrosion products and eventual damage of the surrounding concrete. The actual form that long term corrosion product accumulation will take is not known, but a working hypothesis will be made that the products would spread around the break over a region comparable to the size of the rebar diameter. Thus the expansion-related damage will be calculated as if it would result from spreading the total metal loss at the break over an area equal to that of the cut end of the rebar. Consequently, the calculated anodic current at the break was divided by $\pi\phi^2/4$ to obtain a nominal corrosion rate i_n which was calculated for each case and shown in Figure 20 as function of cladding break radius and concrete resistivity. The value of i_n increased with increasing break size, and decreased with increasing concrete resistivity, in both instances following roughly a power law with exponent close to unity indicating that these parameters are critical to the predicted rate of damage. The sensitivity of the output to the assumed value of i_{oa} or i_{oc} was evaluated with results shown Figure 21, showing relatively minor effects compared to those from changing concrete resistivity or size of cladding break.

The present resistivity and size dependence trends are in agreement with our previous work in which a cruder model for evaluating macrocell coupling was used ⁽¹⁸⁾. However, mainly because of coarser discretization, the total anodic break current estimated by the previous model was consistently about 2 to 3 times greater than in the present case. The present calculations consider coupling of the break only with a 1m portion of the rebar assembly, and a relatively small volume of concrete. However, as the macrocell currents decay very rapidly with distance to the break, only marginal gain in significance is expected by extending the model to a larger size assembly especially considering the inherent uncertainty in the values of all the other parameters. It may be argued also that small cladding breaks are likely to occur in multiple spots in a typical structural element, so that characteristic distances between breaks in the order of 1 m would be likely thus justifying limiting the simulated region size accordingly.

Service Life Implications

The service life T of a reinforced concrete structure is often estimated using the general approach proposed by Tuutti ⁽²¹⁾:

$$T=T_1 + T_2 \tag{5}$$

where T_1 is the length of the corrosion initiation period, and T_2 is the corrosion propagation time (from start of active corrosion until cracking of the concrete cover is observed).

A rough estimate of T_2 may be made by

$$T_2 = \frac{2F\rho_s X_{crit}}{i_{eff} A_w} \tag{6}$$

where X_{crit} is the amount of corrosion penetration needed to cause an observable crack ⁽²²⁾, i_{eff} is the average rate of corrosion of a rebar, F is Faraday's constant, and ρ_s and A_w are the density and atomic weight of iron, which is assumed to corrode as divalent cations. There is little information on the value

of X_{crit} under corrosion localization conditions, but recent work has shown that for a limited range of dimensions and for corrosion occurring on the side surface of a rebar:

$$X_{crit} \sim 0.011 \cdot \left(\frac{C}{\phi}\right) \cdot \left(\frac{C}{L_c} + 1\right)^{1.8} \quad (\text{mm}) \quad (7)$$

where C is the concrete cover thickness, ϕ is rebar diameter and L_c is length of the corroding rebar section. ^(18,22)

Assuming that the rebar-end corrosion effects are roughly similar to those of corrosion on the side surface, application of Eq. (7) to the base case ($C=7.5$ cm, $\phi=L_c=2$ cm and $r_o=0.05$ cm) and assuming $i_{eff} = i_n$, yields $X_{crit} \sim 0.7$ mm. This value is only nominal as it involves extrapolation beyond the range of conditions used to develop Eq. (7). Nevertheless, the large estimated value of X_{crit} reflects the mitigating effect of limiting corrosion to a relatively small area beneath a thick concrete cover ⁽²²⁾. For the base case with high quality concrete of $\rho=30$ k Ω .cm, Eqs (6) and (7) project a value $T_2 \sim 100$ years. This good prognosis derates rapidly if r_o increases or ρ decreases. Thus, tolerance to a cladding break appears promising as long as the break is small (e.g. <1 mm diameter) and the concrete resistivity is high. The potential beneficial effects of corrosion product plugging of the break will be discussed in Ref. 20.

The above analysis represents sweeping assumptions that need refinement in the future. To that effect, continuing detailed characterization of the corrosion behavior of SCR in actual concrete service is needed. Corrosion product-induced changes in concrete resistivity around the break, which may significantly affect the extent of macrocell coupling, should be examined. The projection to obtain X_{crit} involved large extrapolation and assumed that the accumulation of corrosion products in the present case roughly corresponded to that used to formulate Eq. (7). An actual system would deviate greatly from the assumed case; for example rebar cut ends often face away from the concrete surface, which would result in a less severe situation than assumed. Other factors, such as preexisting concrete cracking could represent instead an aggravating factor not considered here. Additional testing and modeling is in progress to address some of these issues.

CONCLUSIONS

1. Stainless steel clad rebar (SCR) with isolated ends or terminated with either a stainless steel (SS) cap or welding overlay had high corrosion resistance in liquid solution with extremely high chloride levels ($\sim 5M$ Cl⁻). SCR with isolated ends or terminated with a SS cap remained passive in concrete with up to 8% Cl⁻ by weight of cement for about 1 year.
2. Stainless steel clad rebar with isolated ends in saturated Ca(OH)₂ solution with $\sim 5M$ Cl⁻ at 40 °C remained passive for more than 6 months. The potentials in concrete with 8% (of cement weight) chloride dropped significantly after they were moved from room temperature exposure into a 40 °C chamber at 100% RH. However, no other evidence of active corrosion was detected during the limited subsequent test period. Testing under these conditions continues.
3. Stainless steel clad rebar with 1 mm ϕ hole drilled through the cladding corroded actively in saturated Ca(OH)₂ solution with $\sim 5M$ Cl⁻. In concrete with 8% chloride, only one of a duplicate pair of specimens with clad breaks showed clear signs of corrosion initiation after 100 days, and even in that case there were signs of subsequent recovery.

4. Modeling calculations indicated that the corrosion rate of exposed carbon steel in stainless steel clad rebar depended strongly on resistivity of concrete and clad break size. Better quality (higher resistivity, e.g. ≥ 30 k Ω .cm) concrete and smaller imperfection sizes were projected to significantly reduce corrosion. The calculations suggested that widely spaced cladding breaks of sub-millimeter size would be tolerable in concrete that retains high resistivity.

ACKNOWLEDGEMENT

The authors would like to thank Dr. S.C. Kranc for his suggestions on the implementation of the corrosion model. This work was supported by Stelax (U.K.) Limited. The findings and opinions expressed in this paper are those of the authors and not necessarily those of the supporting organization.

REFERENCES

1. G.N. Flint, R.N. Cox, Magazine of Concrete Research 40, 142 (March 1988): p.13.
2. R.N. Cox, J.W. Oldfield, "The Long Term Performance of Austenitic Stainless Steel in Chloride Contaminated Concrete," Proceedings of the Fourth International Symposium on Corrosion of Reinforcement in Concrete Construction, Eds. C.L. Page, P.B. Bamforth and J.W. Figg, (Cambridge, UK: Society of Chemical Industry, 1996), p. 662.
3. U. Nurnberger, "Corrosion Behavior of Welded Stainless Steel Reinforced Steel in Concrete," Proceedings of the Fourth International Symposium on Corrosion of Reinforcement in Concrete Construction, Eds. C.L. Page, P.B. Bamforth and J.W. Figg, (Cambridge, UK: Society of Chemical Industry, 1996), p. 623.
4. P. Pedferri, L. Bertolini, F. Bolzoni, T. Pastore, "Behavior of Stainless Steels in Concrete," Proceedings of the International Seminar: The State of the Art of the Repair and Rehabilitation of Reinforced Concrete Structures, Eds. W.F. Silva-Araya, O.T. DE RINCÓN, and L. P. O'Neill, (Reston, VA: ASCE, 1997): p.192.
5. D.B. McDonald, D.W. Pfeifer, M.R. Sherman, "Corrosion Evaluation of Epoxy-Coated, Metallic-Clad and Solid Metallic Reinforcing Bars in Concrete," U.S. Dept. of Transportation: Federal Highway Administration Report, Publication No. FHWA-RD-98-153, 1998
6. J. Hewitt, M.Tullmin, "Corrosion and Stress Corrosion Cracking Performance of Stainless Steel and Other Reinforcing Bar Materials in Concrete," Proceedings of International Conference: Corrosion and Corrosion Protection of Steel in Concrete, Ed. K. N. Swamy, (Sheffield, UK: Sheffield Academic Press, 1994): p. 527.
7. NUOVINOX, Product Information, (West Glamorgan, U.K.: Stelax (U.K.) Limited, 1998)
8. A. Zayed, A. Sagüés, R. Powers, "Corrosion of epoxy-coated reinforcing steel in concrete," Corrosion/89, paper No. 379, (Houston, TX: NACE International, 1989)
9. A. Zayed, A. Sagüés, Corrosion Science 30, 10 (1990): p. 1025.
10. W. Stumm, J. J. Morgan, Aquatic Chemistry, (John Wiley & Sons, Inc, 1996): p. 157

11. P. Castro, A. Sagüés, E. I. Moreno, L. Maldonado and J. Genesca, Corrosion 52, 8(1996): p. 609
12. D.A. Jones, Principles and Prevention of Corrosion, (New York: Macmillan Publishing Company, 1992): p. 147.
13. Florida Standard Specifications for Road and Bridge Construction 2000, Section 346: Portland Cement Concrete
14. Personal Communication with Corrosion Laboratory of Florida Department of Transportation
15. S. Goñi and C. Andrade, Cement and Concrete Research 20, 4(1990): p525
16. J.P. Broomfield, Corrosion of Steel In Concrete, (E & FN SPON, 1997): p17
17. S. Goni, C. Alonso, E. Menendez, A. Hidalgo and C. Andrade, "Microstructural Characterization of The Carbonation of Mortar Made With Fly Ashes", Proceedings of 10th International Congress on the Chemistry of Cement, 10th, Ed: H. Justnes, (Goeteborg, Swede: Amarkai AB, 1997)
18. F. Cui, A. Sagüés, "Corrosion Behavior of Stainless Steel Clad Rebar", Corrosion/2001, paper No. 0146, (Houston, TX: NACE International, 2001)
19. S. Kranc, A. Sagüés, "Calculation of Extended Counter Electrode Polarization Effects on the Electrochemical Impedance Response of Steel in Concrete", ASTM STP 1188, Eds.: J. Scully, D. Silverman, M. Kendig, (Philadelphia, PA: ASTM, 1993)
20. F. Cui, A. Sagüés, paper to be published
21. K. Tuutti, Corrosion of Steel in Concrete, (Stockholm, Sweden: Swedish Cement and Concrete Research Institute, S-100 44, 1982)
22. A.A. Torres-Acosta, A. Sagüés, "Concrete Cover Cracking with Localized Corrosion of Reinforcing Steel," Proceedings of the 5th CANMET/ACI International Conference on Durability of Concrete, SP-192, Ed. V.M. Malhotra, (Farmington Hills, Mich: American Concrete Institute, 2000): p. 591.

TABLE 1
CHEMICAL COMPOSITION AND PH VALUES OF TEST SOLUTIONS (g/L)

	Ca(OH) ₂ *	NaOH	KOH**	Na ₂ CO ₃	NaHCO ₃	pH***
SCS	2.0	-	-	-	-	12.6
SPS	2.0	8.33	23.3	-	-	13.6
CPS	-	-	-	4.21	2.66	9.7

*Most of the Ca(OH)₂ was not dissolved

**Reagent grade KOH had only a purity of 85.3%

*** These are pH values before addition of Cl⁻

TABLE 2
POLARIZATION PARAMETERS CHOSEN FOR THE CALCULATIONS

	$E_{oa,c}$ (V vs SCE)	$i_{oa,c}$ ($\mu\text{A}/\text{cm}^2$)	$b_{a,c}$ (V/dec)
Anodic	-0.86	$5 \cdot 10^{-5} *$	0.06
Cathodic	0.10	$1 \cdot 10^{-5}$	0.10

* $i'_{oa} = 4i_{oa}$ (see text)

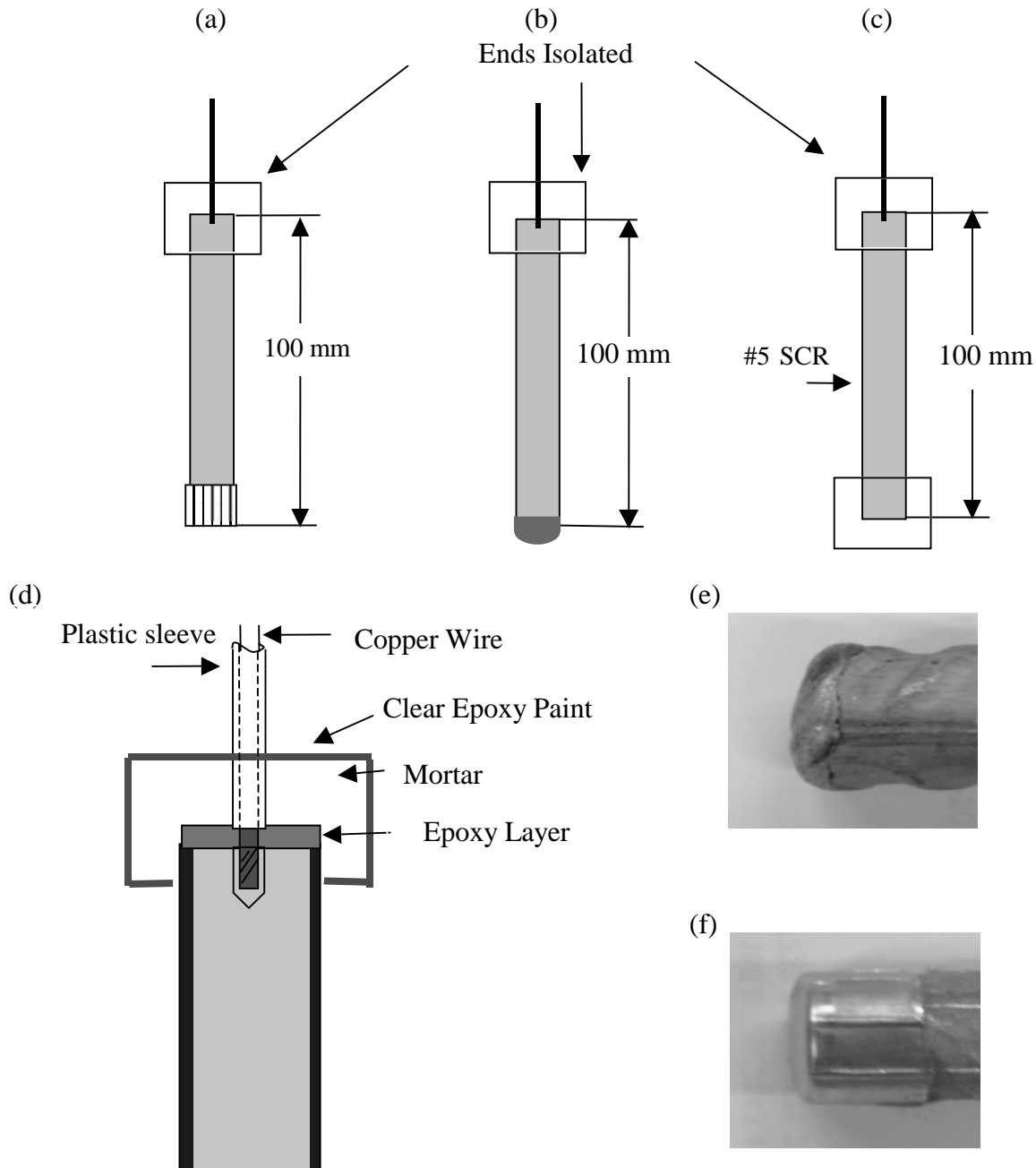
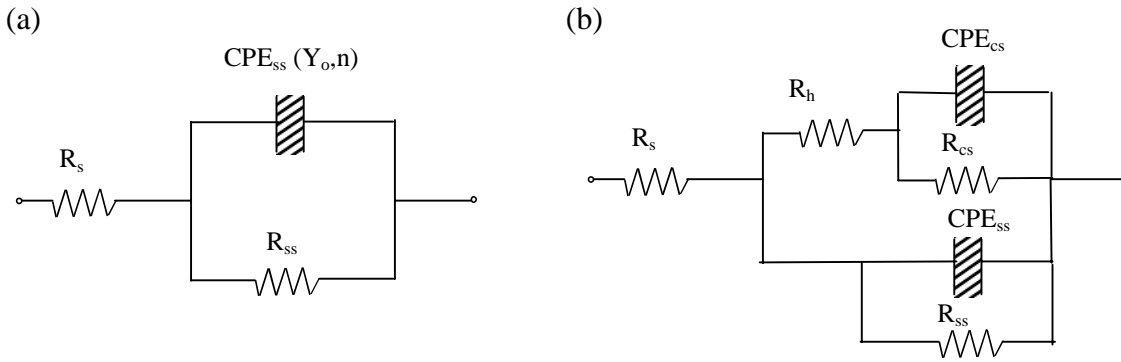


FIGURE 1- SCR specimens, classified based on cut-end termination methods (Each specimen has one cut-end terminated with a mortar cap): a, Type A—terminated with a SS cap; b, Type B—terminated with a welding overlay; c, Type C—End isolated with a mortar cap; d, End isolation detail; e, a typical welding overlay; f, a typical SS cap



R_s : solution resistance
 R_{cs} : polarization resistance of CS
 R_{rust} : resistance of corrosion product
 CPE : constant phase-angle element ($Z=Y_o^{-1}(j\omega)^{-n}$), cs-carbon steel, ss-stainless steel,
 R_h : resistance of solution at the small hole
 R_{ss} : polarization resistance of SS

FIGURE 2 - Equivalent circuit used to interpret the EIS results: a, model for passive SCR with cladding breaks; b, model for SCR with a 1mm ϕ hole

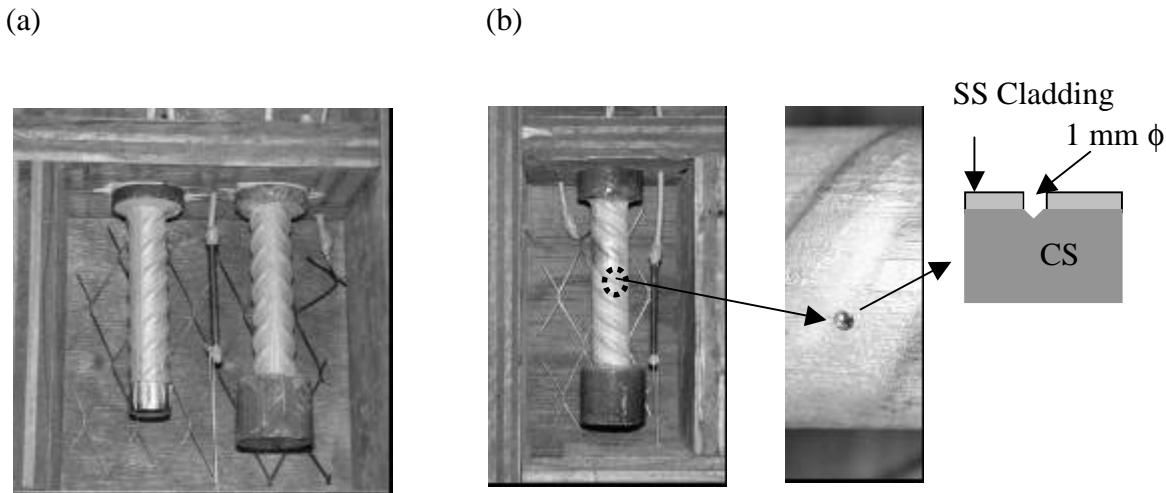
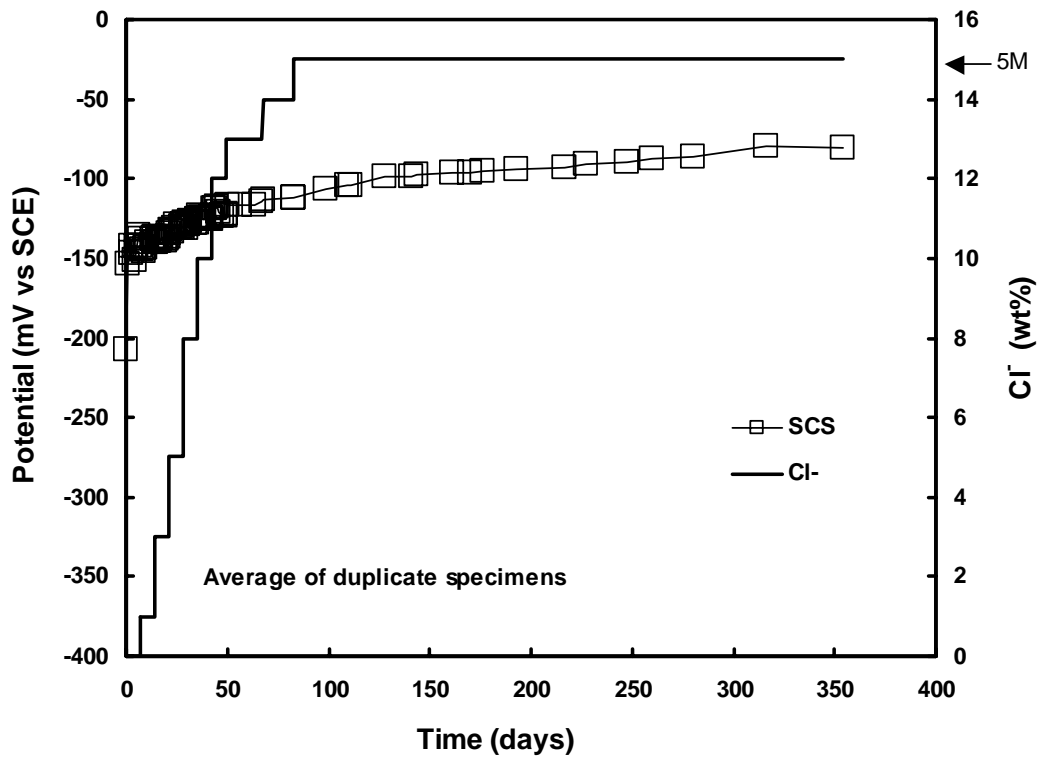


FIGURE 3- Concrete specimen layout: a, SCR without cladding break; b, SCR with a 1mm ϕ hole

(a)



(b)

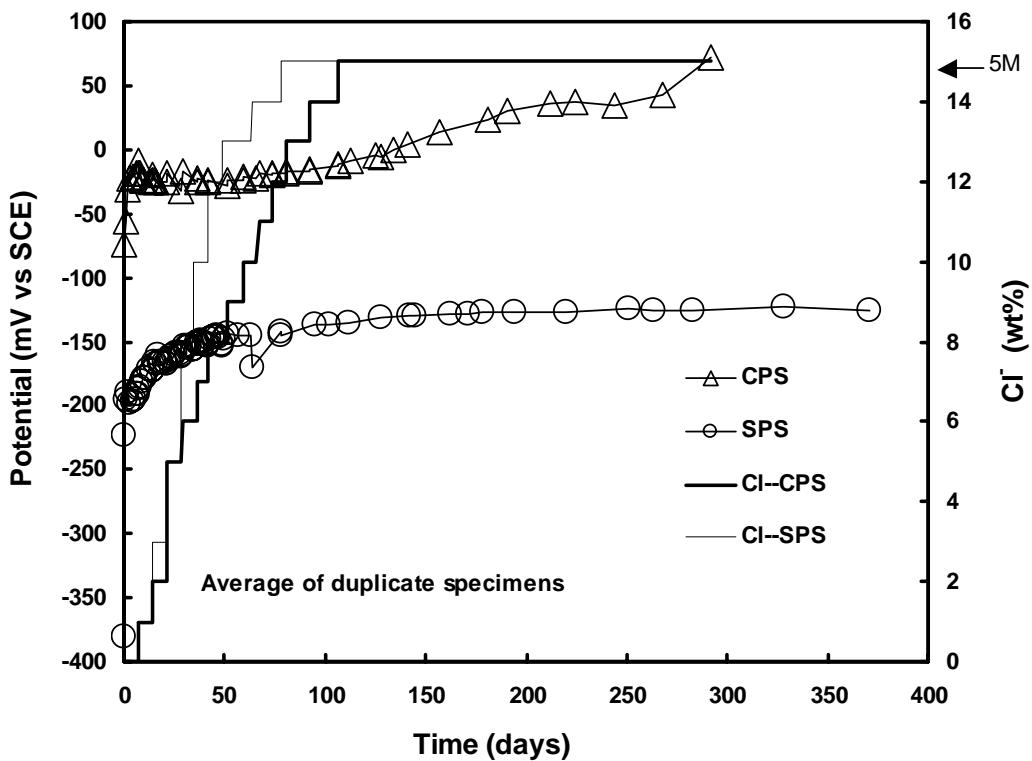


FIGURE 4- E_{oc} of SCR with isolated ends in various solutions: a, SCS-pH~12.6; b, CPS-pH~10; SPS-pH~13.6. Solid step lines denote chloride concentration (right ordinate axis).

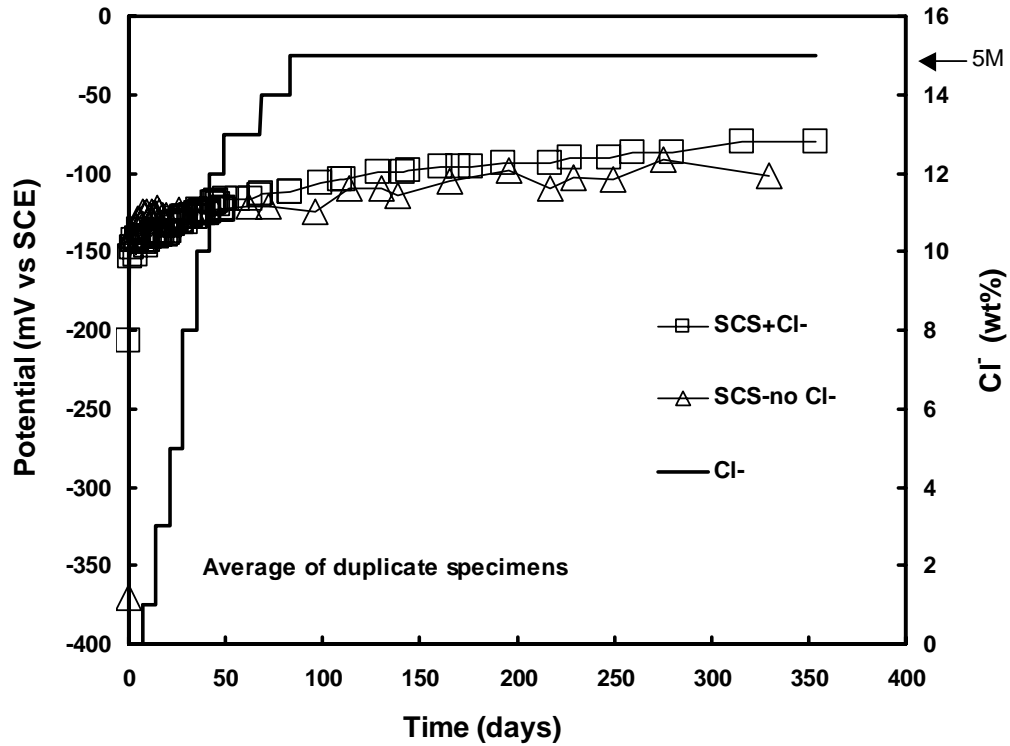


FIGURE 5- E_{oc} of SCR with isolated ends in liquid solutions illustrating behavior with and without chloride ions. Solid step line denotes chloride concentration (right ordinate axis).

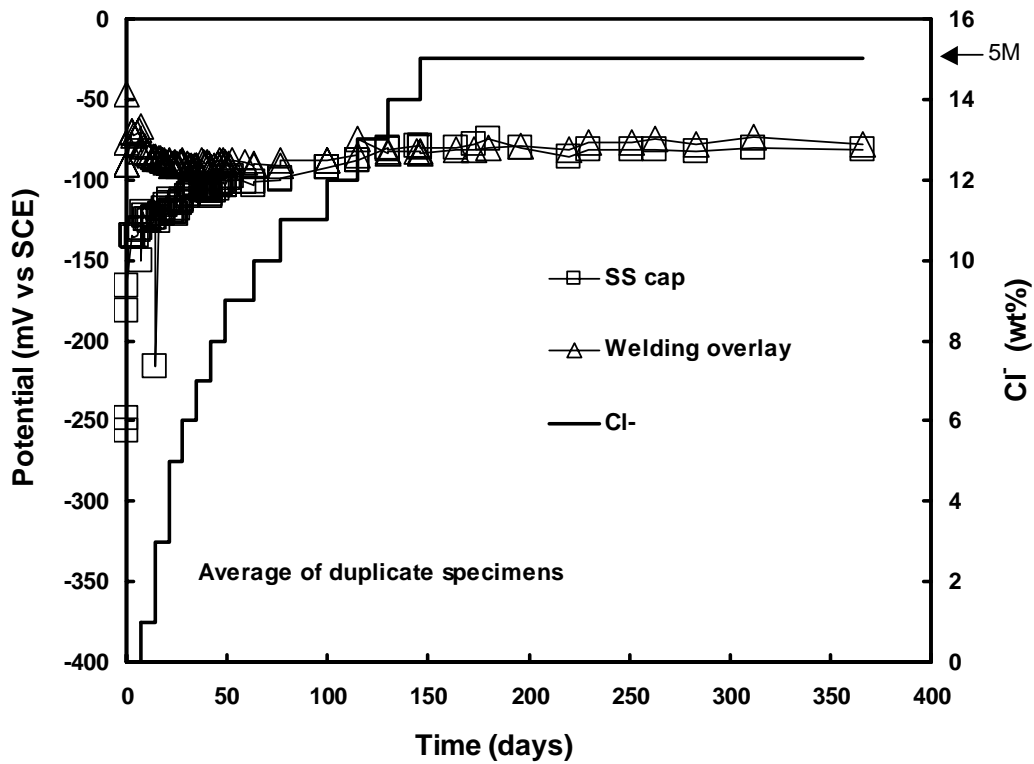


FIGURE 6- E_{oc} of SCR with different end termination methods immersed in SCS. Solid step line denotes chloride concentration (right ordinate axis).

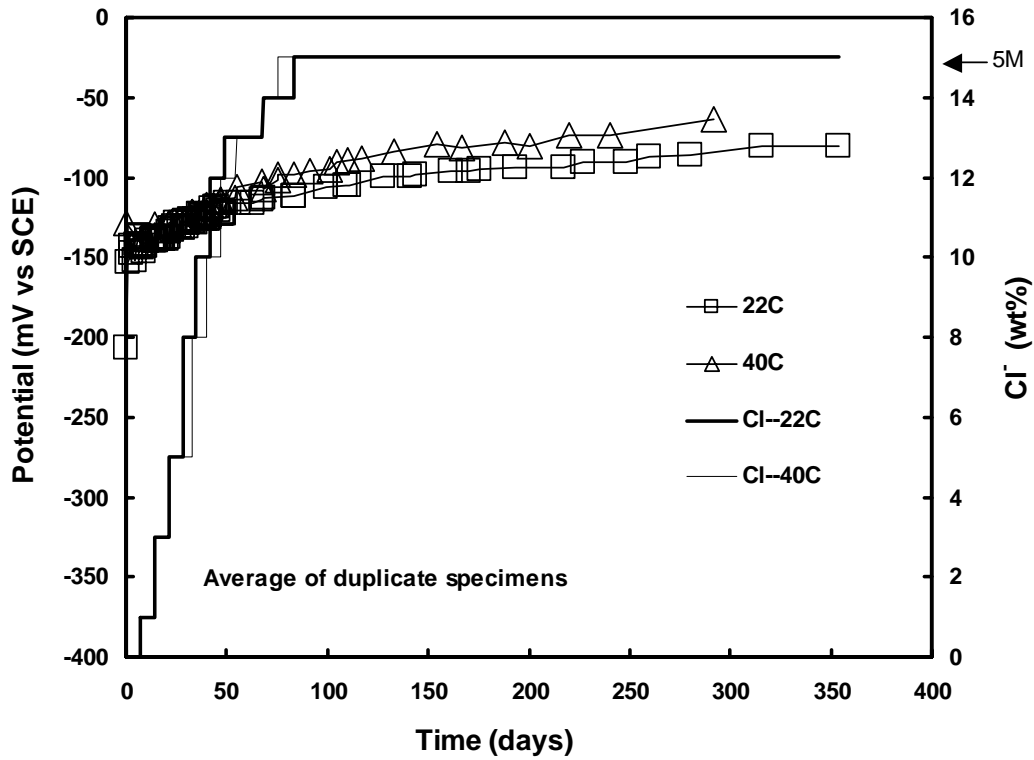


FIGURE 7- E_{oc} of SCR with isolated ends in SCS at different temperatures. Solid step lines denote chloride concentration (right ordinate axis).

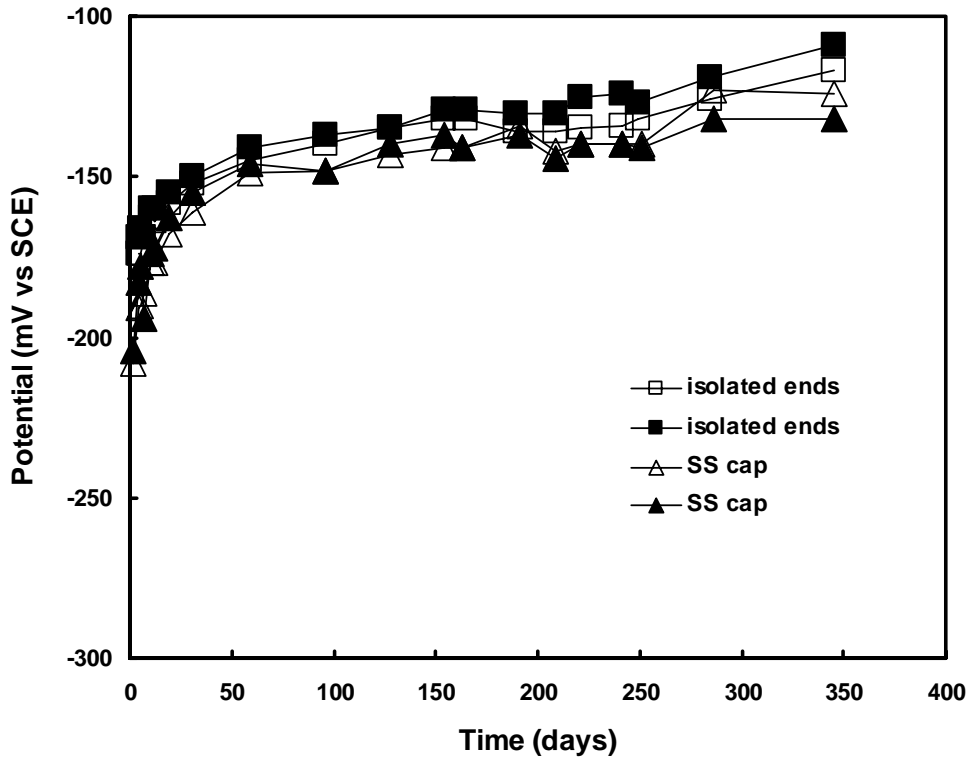


FIGURE 8- E_{oc} of SCR in concrete with 5% chloride (no cladding breaks)

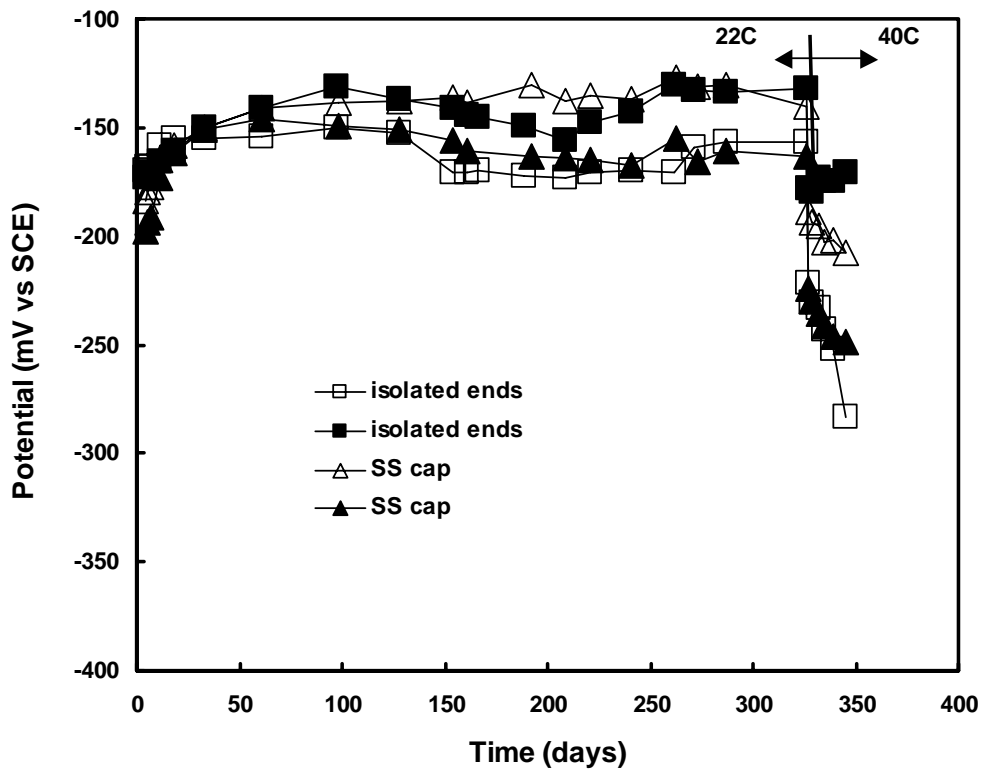


FIGURE 9- E_{oc} of SCR in concrete with 8% chloride (no cladding breaks)

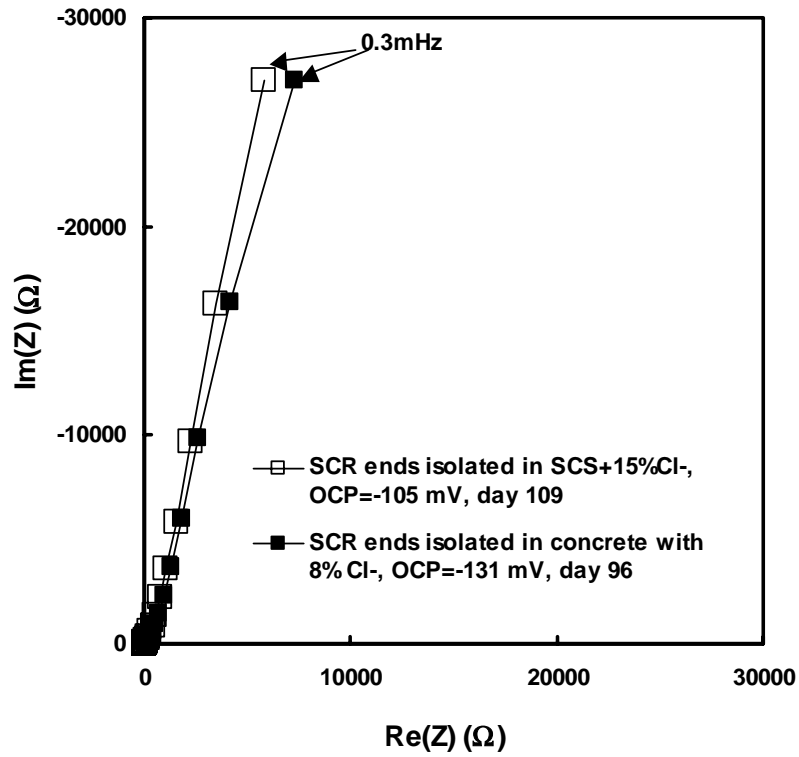


FIGURE 10-Typical EIS of SCR with isolated ends (surface area is $\sim 40 \text{ cm}^2$)

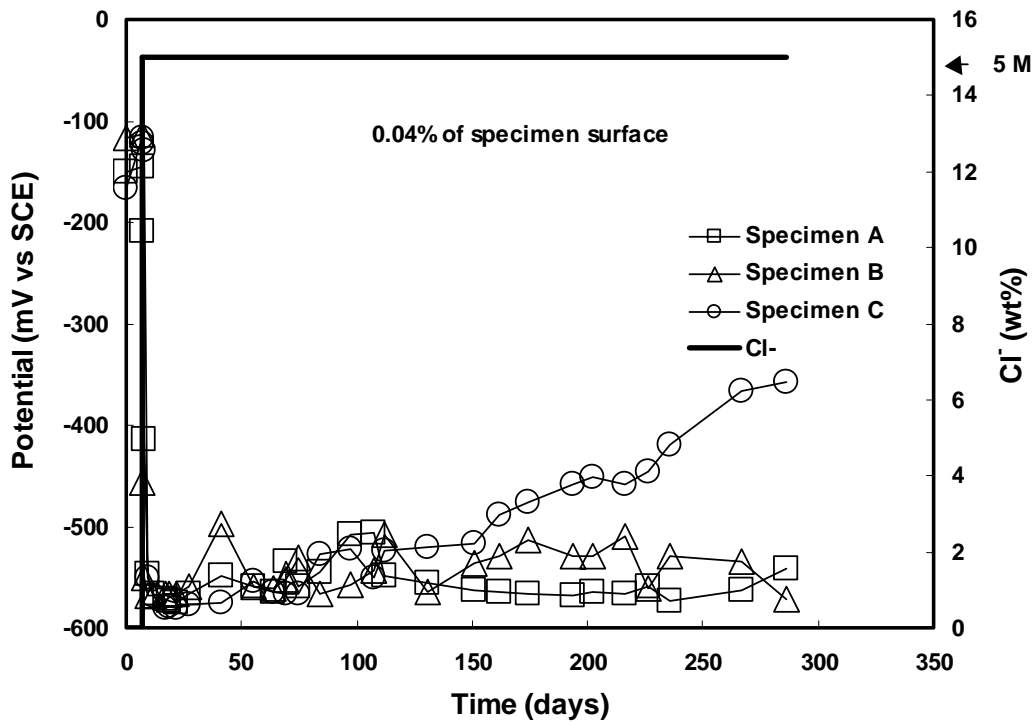


FIGURE 11- E_{oc} of SCR with 1mm ϕ hole in SCS with 15 wt% chloride. Solid step line denotes chloride concentration (right ordinate axis).

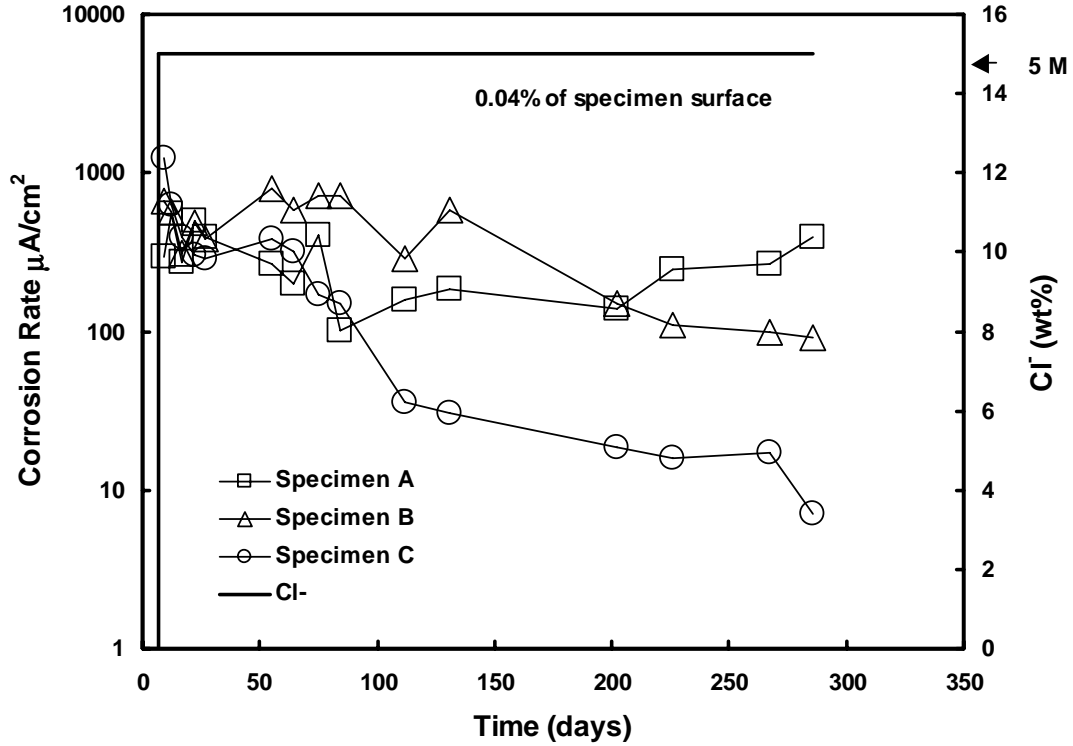


FIGURE 12-Corrosion behavior of SCR with 1mm ϕ hole in SCS with 15% chloride. Solid step line denotes chloride concentration (right ordinate axis).

(a)



(b)

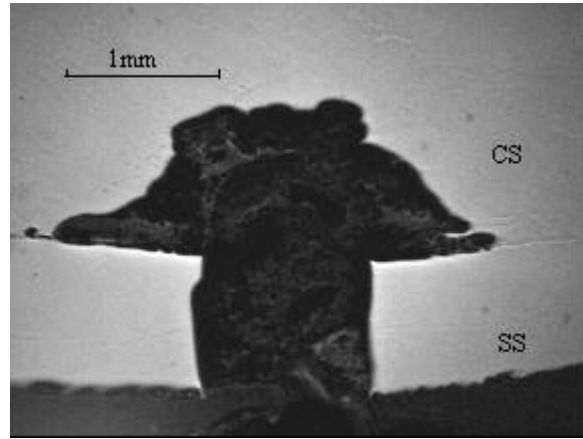


FIGURE 13-a, the corrosion appearance of SCR; b, metallographic cross-section of the drilled at the end of test (test solution was SCS with 15% chloride, specimen A)

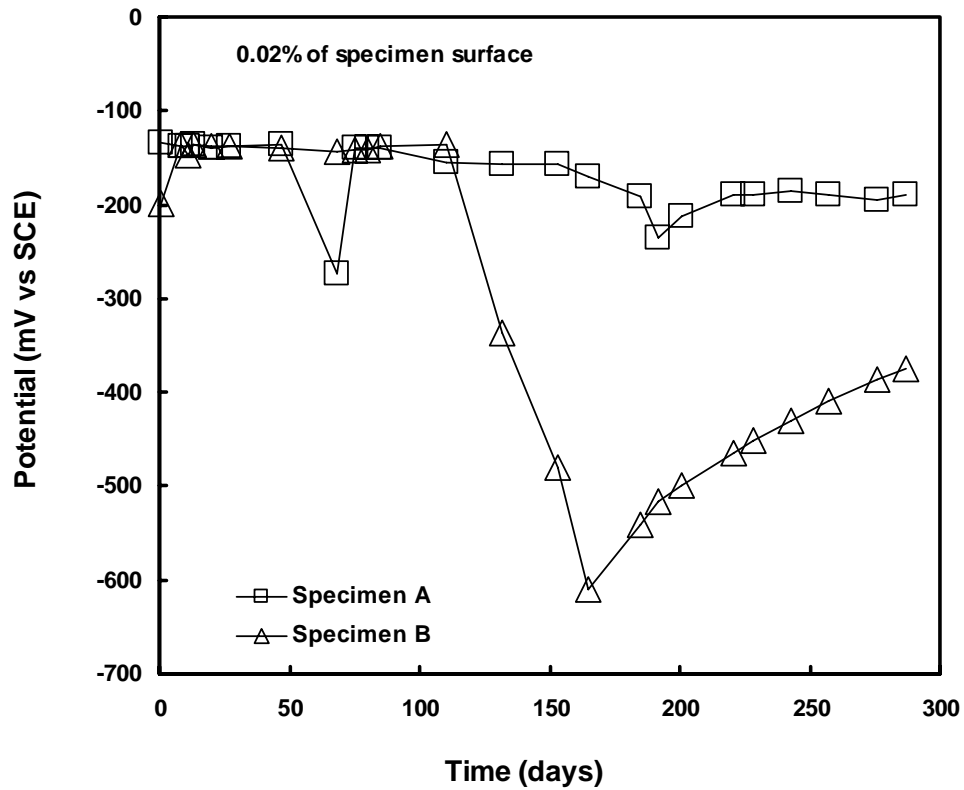


FIGURE 14- E_{oc} of SCR with 1mm ϕ hole in concrete with 8% chloride

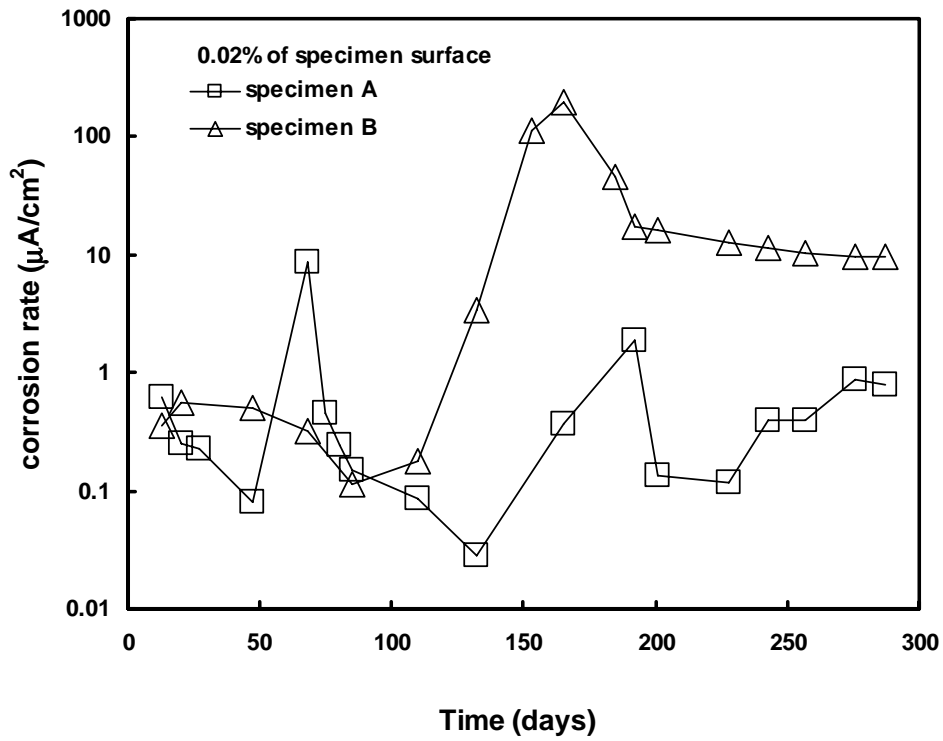


FIGURE 15- Corrosion behavior of SCR with 1mm ϕ hole in concrete with 8% chloride

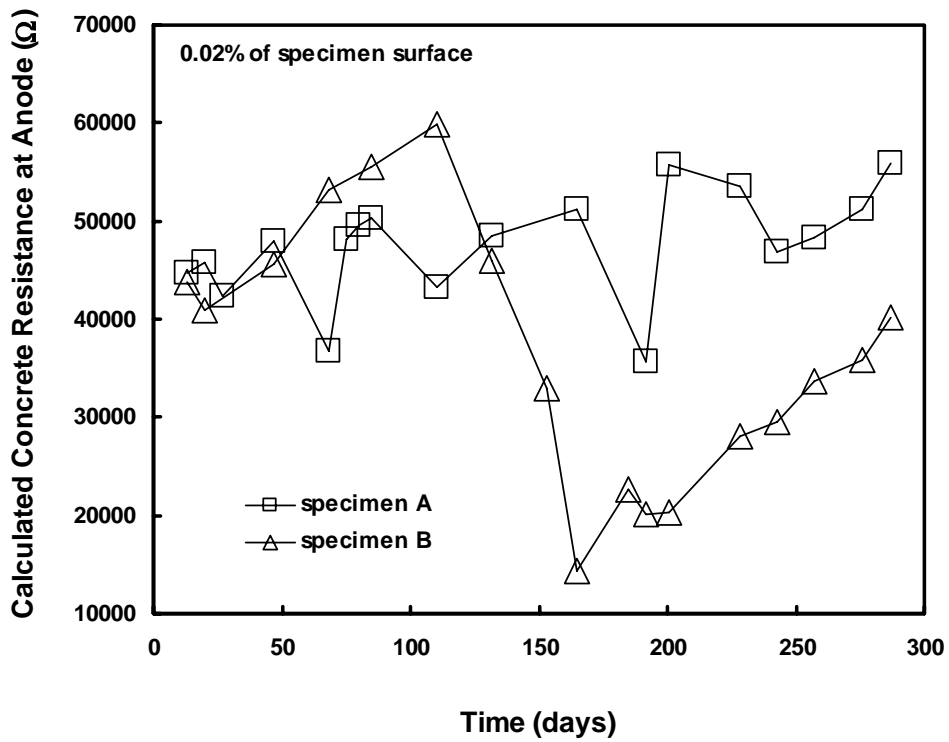


FIGURE 16- Calculated concrete resistance at the anode, R_h

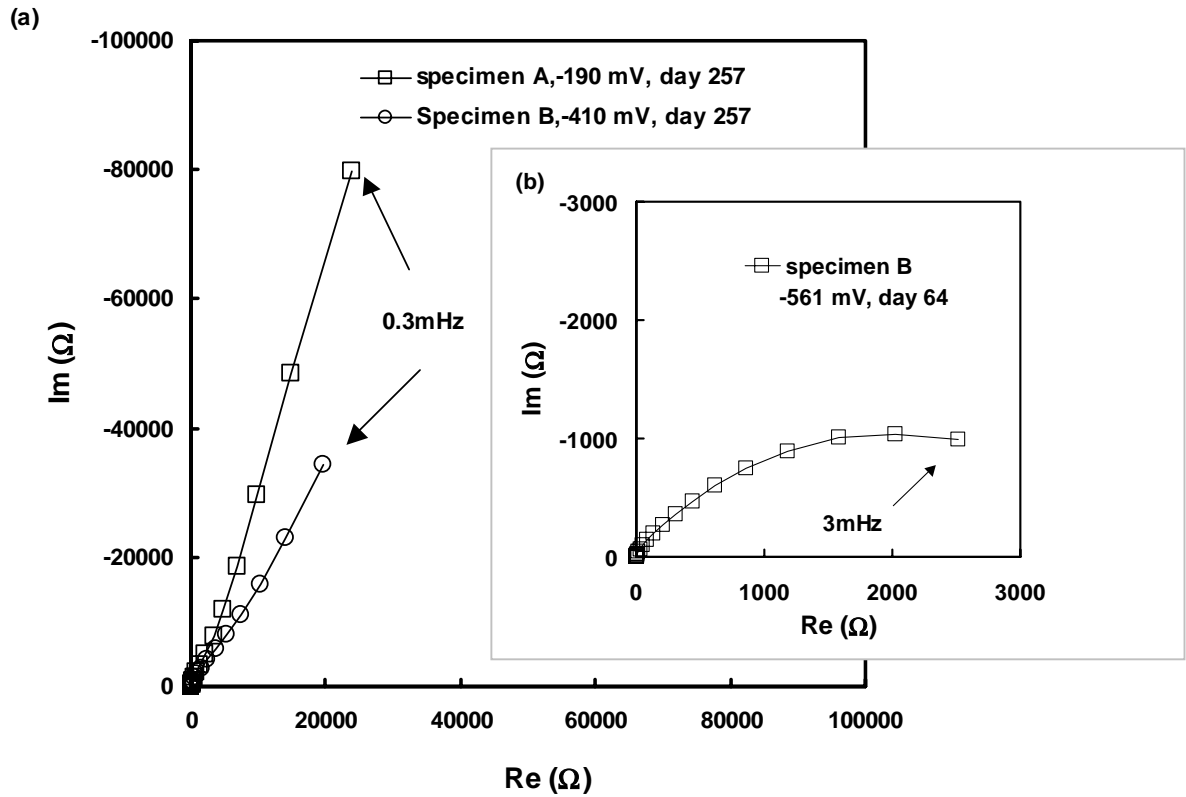


FIGURE 17-Typical EIS diagram of SCR with 1mm ϕ hole: a, SCR in concrete, surface is $\sim 40 \text{ cm}^2$; b, SCR in SCS+15 % Cl^- , surface is $\sim 20 \text{ cm}^2$

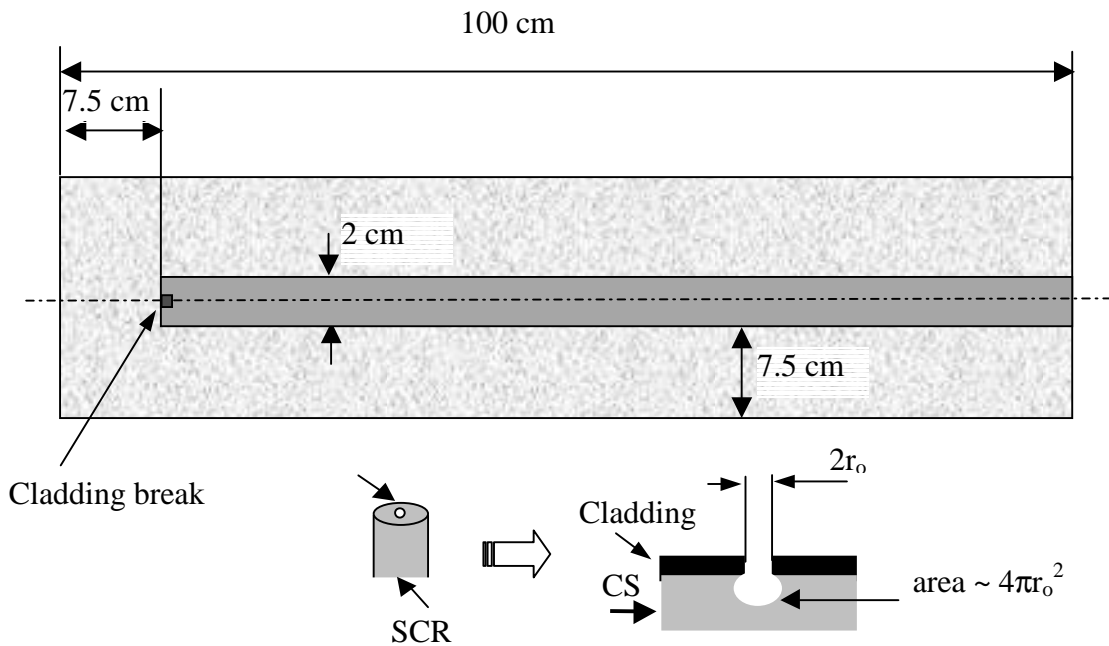


FIGURE 18-Longitudinal cross-section of the cylindrical reinforced concrete system for modeling

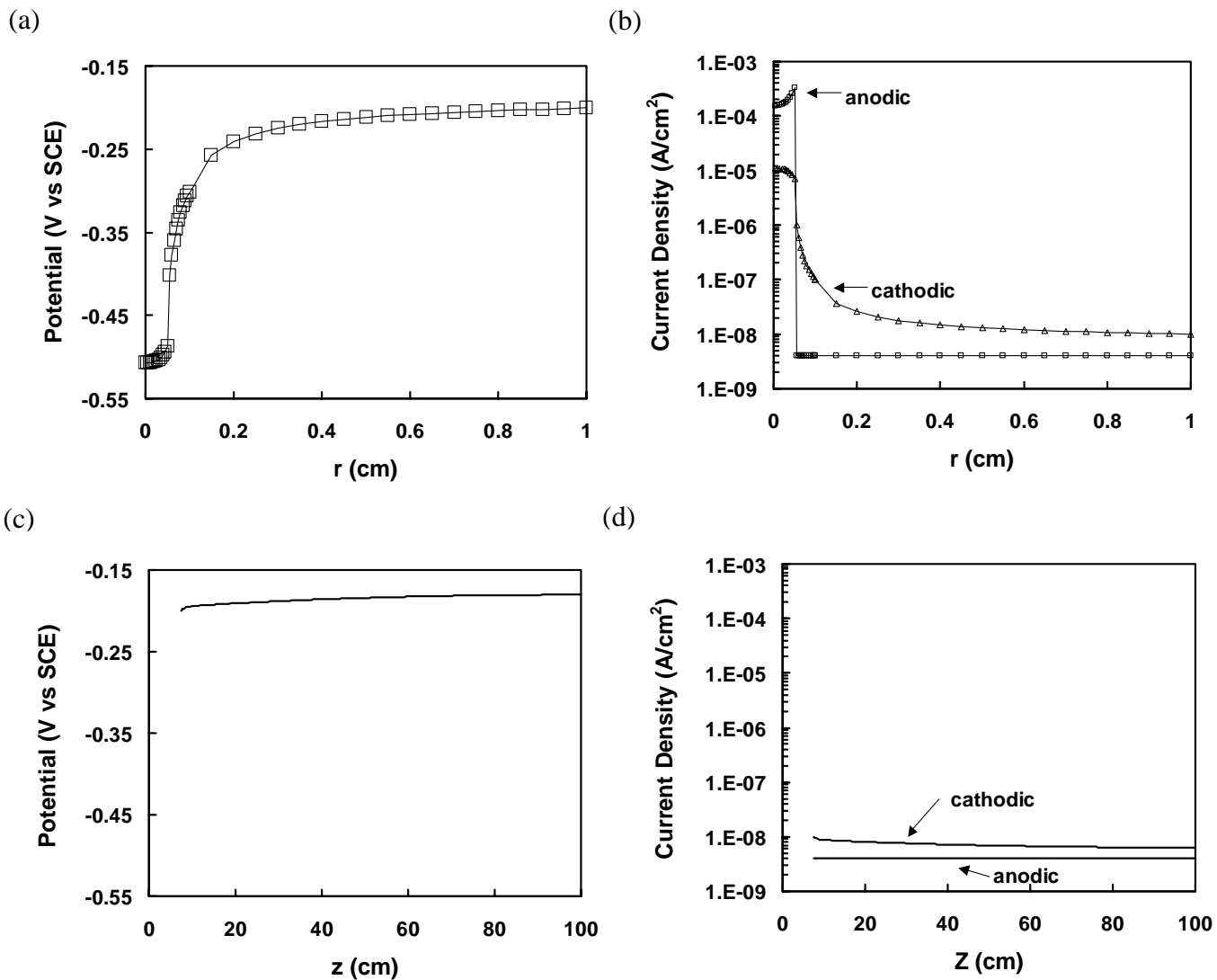


FIGURE 19-a, potential distribution at bar end; b, current density distribution at bar end; c, potential distribution at bar side surface; d, current density distribution at bar side surface (control case)

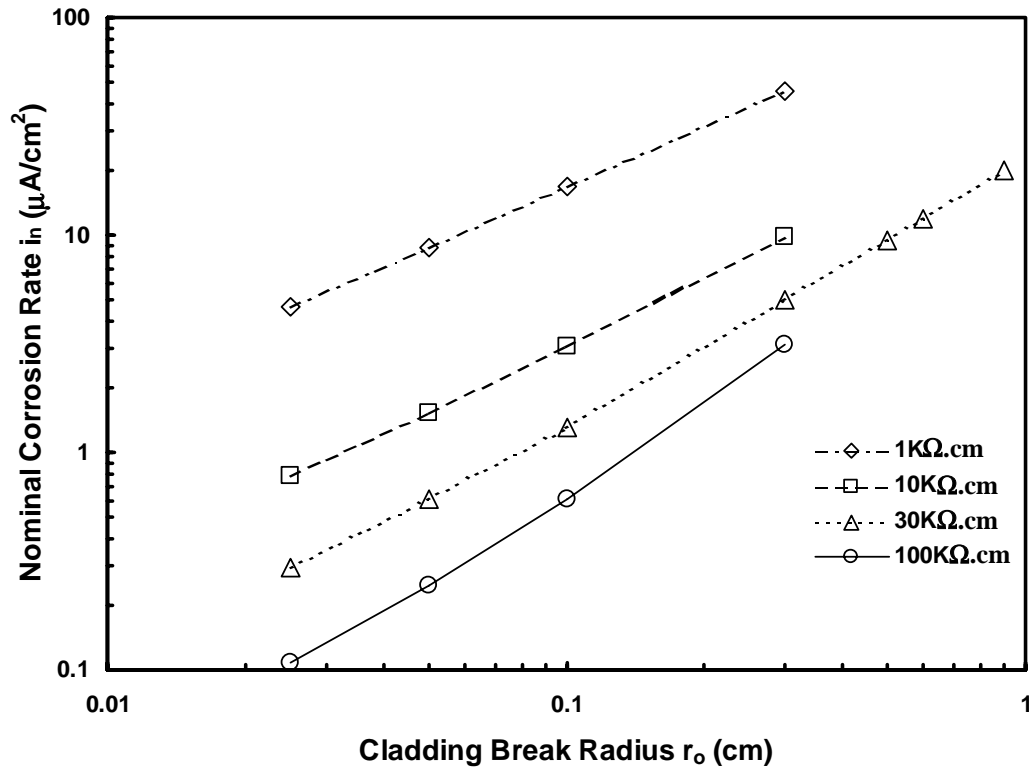


FIGURE 20-Effect of concrete resistivity and break size on the nominal corrosion rate of the rebar end

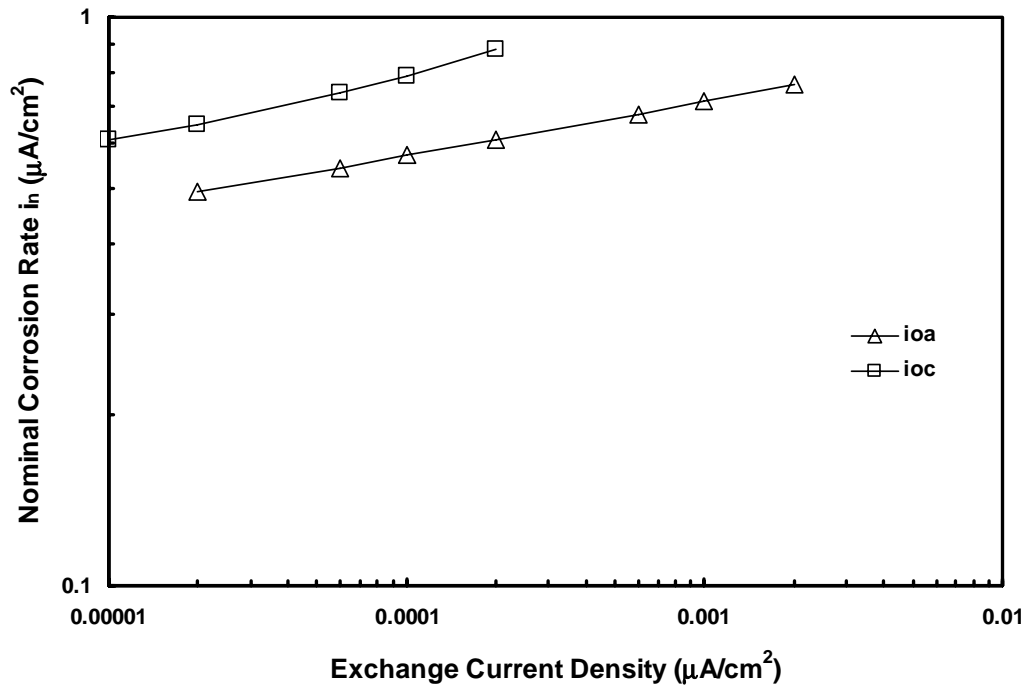


FIGURE 21-Effect of exchange current density of anode and cathode on the nominal corrosion rate of the rebar end